


**Experimental Characterization of Tunable Vector Beam Decoder  
for High-dimensional Quantum Key Distribution using Spatial  
Modes of Light**

*Master's Thesis*

William A. Jarrett  
Department of Electrical Engineering  
Stanford University

May 17th, 2024

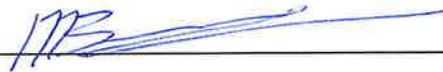
I certify that I have read this thesis and that, in my opinion, it is fully adequate in scope and quality as a thesis for the degree of Master of Science in Electrical Engineering with Distinction in Research.



Professor Jelena Vučković

Primary Advisor, Department of Electrical Engineering

I certify that I have read this thesis and that, in my opinion, it is fully adequate in scope and quality as a thesis for the degree of Master of Science in Electrical Engineering with Distinction in Research.



Professor Mark Brongersma

Secondary Advisor, Department of Materials Science and Engineering

## Abstract

To meet the growing need of advancements in data encryption and cryptography, many researchers have turned to using quantum-based encryption, which use the fundamental laws of physics to provide unconditional security. One such encryption method is Quantum Key Distribution (QKD), which is able to securely create a cryptographic key while revealing the presence of an eavesdropper through the no-cloning theorem. This theorem states that if an attempt to measure or clone the transmitted information is made, the eavesdropper will inherently change the quantum state of the signal, collapsing the wave function and inducing detectable error. Standard QKD protocols rely on transmitting information with 1 bit/photon with the information being encoded in the photon's degrees of freedom, such as its polarization. Due to its capacity to enable a higher information capacity and increase resilience to noise, high-dimensional (HD) QKD has attracted considerable attention and typically utilizes the spatial modes of light. However, the implementation of HD QKD with spatial modes is challenged by a need for special-purpose devices, which are ideally simple to integrate into current systems. A proposed solution is to create an HD QKD device making use integrated silicon photonics, which are easy to commercially fabricate. Following this, a tunable device to perform HD QKD is inversely designed and termed a vector beam emitter (VBE) or vector beam decoder (VBD), depending on how the device is used. This thesis experimentally evaluates the tunable VBD for HD QKD utilizing 3D-polarized spatial modes. Evaluation is performed by using the VBD to decode spatial modes of light sent to the device, verifying the working principle of the device. Additionally, we investigate its ability to perform QKD by computing two QKD transfer matrices, the first in the case of simulating focused ideal scalar and vector input modes and the second by using the experimental results. From these transfer matrices, we calculate the security values, providing insight into the device's potential performance for QKD. In the case of simulated focused input beams, we report a quantum error rating of 0.1393 and 0.3935 bits/photon. In the experimental case we report a quantum error rating of 0.4234 and -1.3082 bits/photon. This demonstrates a proof-of-concept that the VBD works as intended and that an HD QKD system utilizing the spatial modes of light could be implemented. Further study should look at implementing a full VBE/VBD system to avoid errors induced in focusing encoded input beams on the VBD and improving overall performance.

## Key Words

High-dimensional quantum key distribution, structured light, orbital angular momentum, nanophotonics, inverse design, integrated photonics

## **Acknowledgements**

To Prof. Jelena Vučković for supporting and advising this project and my thesis. I really appreciate your willingness to provide me an opportunity to do meaningful research as a Master's student.

To Prof. Mark Brongersma for supporting this collaboration and for his willingness to serve as the second reader for my thesis.

To Dr. Eileen Otte, whose assistance, guidance, and support have been invaluable. I could not have done it without you, and I am really grateful for all the time you have given me!

To Dr. Alex White, Geun Ho Ahn, and Dr. Kasper Van Gasse for being so supportive when I joined the lab group, teaching me so much and helping me to find this project.

To Dr. Giovanni Scuri and Sungjun Eun for fabricating the VBE/VBD. I cannot thank both of you enough for being willing to take time away from your own projects to perform this fabrication for us!

To Prof. Gordon Wetzstein and his lab group for allowing us to borrow their SLM for this project.

## Table of Contents

<b>Abstract and Keywords</b> .....	<b>1</b>
<b>Acknowledgements</b> .....	<b>2</b>
<b>Thesis</b>	
<b>1. Introduction</b> .....	<b>4</b>
<b>2. Background Information for Quantum Key Distribution System</b> .....	<b>6</b>
A. Performing Polarization-based Quantum Key Distribution.....	6
B. High-dimensional Quantum Key Distribution with Spatial Modes of Light .....	7
C. Design and Implementation of the Tunable Vector Beam Decoder/Encoder .....	8
D. Simulated Results of Tunable Vector Beam Emitter / Vector Beam Decoder .....	10
<b>3. Experimental Process</b> .....	<b>10</b>
A. Device Fabrication .....	10
B. Measurement of Vector Beam Decoder Device .....	11
C. Experimental Set-up.....	12
<b>4. Results and Analysis</b> .....	<b>14</b>
<b>5. Conclusion and Future Work</b> .....	<b>20</b>
<b>6. References</b> .....	<b>20</b>

## 1. Introduction

There is an increasingly large demand for faster data processing techniques to meet the requirements of various applications in both the commercial and defense sector, namely for artificial intelligence (AI). This demand has created significant research and improvements into the fields of photonics and quantum computing, taking advantage of the fundamental laws of physics to push data processing speeds past what classical systems are capable of [1]. While this has many positive implications, improvements in data processing necessitate equal improvements in data encryption and cryptography in order to maintain the required level of security. Classical encryption schemes are often unable to maintain this security, turning many researchers to look at quantum-based encryption [2]. One such encryption method is Quantum Key Distribution (QKD), which is able to securely transmit information and reveal the presence of an eavesdropper through the fundamental laws of quantum mechanics, making the quantum signal an ideal trusted courier [3, 4]. Known as the no-cloning theorem, if an attempt to clone the transmitted information is made, the eavesdropper will inherently change the quantum state of the signal [5]. The eavesdropper's presences will also be revealed if an attempt is made to simply measure the state of the transmitted signal, as this will collapse the wave function and induce detectable error at the receiver [6].

QKD schemes have been widely studied, and while they theoretically provide unconditional security over arbitrarily long distances, there are challenges and limitations to practical implementation. First, while QKD generates secure keying material for an encryption algorithm, it does not provide a way to authenticate the source of the QKD transmission. This makes QKD vulnerable to insider threats and would necessitate increased security at the transmission and reception facilities. It is worth noting this challenge is not unique to only QKD encryption schemes, but is something many classical encryption schemes are vulnerable to. However, QKD is uniquely at risk to denial of service attacks due to the no-cloning theorem. While the no-cloning theorem makes it impossible for an eavesdropper to clone information without revealing their presence, the changing of the quantum state also prevents the message from being received by the intended recipient. This provides an adversary with a way to simply stop message transmission if that is their goal. Finally, QKD requires special purpose equipment and typically uses dedicated communication channels, which can make it practically difficult to implement. Traditionally, practical implementation has deviated from the theoretical limits in security, as the tolerance for error in cryptography is very low [7].

A commonly used QKD scheme used is the BB84 protocol, developed by Bennett and Brassard in 1984 [8]. BB84 is a prepare-and-measure protocol that works by using two bases of mutually unbiased basis (MUB) states. This protocol is widely used as the standard protocol for proof-of-concept studies as it is easy to implement and provides a standard for performance to compare within the field of research. There is significant research that looks into improving the performance of QKD in mainly one of two areas: transmission distances [9] and information capacity through high-dimensional (HD) QKD [10]. HD QKD increases the information capacity as increasing the dimension increases the information that can be transmitted per photon [11]. Additionally, it has been shown that HD QKD has an increased robustness to noise, improving the reliability of the system [12]. To accomplish this, many researchers have turned to utilizing spatial modes of light,

such as orbital angular momentum (OAM). OAM and hybrid-OAM polarization modes have been implemented in HD QKD in various media [13-15].

In order to practically implement a QKD scheme utilizing spatial modes, there must be a device capable of preparing and measuring the scalar and vector modes used as the MUB states. As discussed previously, this device must be reliable and secure, and ideally easy to create and implement. Traditionally the preparation and measurement of spatial modes is done with either a spatial light modulator (SLM), digital micromirror device, some combination of q-plates and waveplates, or a mode sorter [14-19]. However, these methods are bulky and challenging to implement on an industrial scale, creating the motivation to design and implement an integrated quantum photonic solution, as this would allow the device to be scaled down in size and cost while improving reliability and compatibility [1, 20]. Within the last decade, there has been several successful demonstrations of implementing QKD through integrated silicon photonics, namely using time-bin and polarization-based QKD, some of which will be detailed below. Silicon typically selected as the primary material for device fabrication because of its well-researched fabrication processes and compatibility with microelectronics leading to easier system integration [21].

In 2017, Sibson et al. demonstrated chip-based QKD using an indium phosphide transmitter chip and a silicon oxynitride receiver chip [22]. This proof-of-concept study demonstrated successful time-bin encoded QKD over a 20 km fiber link using three protocols: BB84, Coherent One Way, and Differential Phase Shift. For BB84, the authors demonstrate an average observed quantum bit error rate (QBER) of 1.05% and an estimated asymptotic secure key rate of 345 kbps. This proof-of-concept provided a performance that was comparable to what was expected in fiber and bulk optical systems at the time, with a low QBER and high key generation rate. However, the use of time-bin QKD limits the system's growth as data transmission requirements increase.

In contrast, Ma et al. in 2016 demonstrated a proof-of-concept study of polarization-based QKD using a silicon photonic transmitter [23]. Polarization-based QKD is often considered better for free-space applications due to their resistance to turbulence in complex media and the lack of birefringence of the atmosphere, but can be more difficult to implement and maintain low error rates in fiber. The authors perform a demonstration of the transmitter using the BB84 protocol over a 5 km long fiber link. They detail a QBER of 5.4% and an asymptotic secure key rate of 0.95 kbps. This work was significant because it represented the first silicon photonic integrated transmitter for polarization-encoded QKD. However, fairly sizable error rates, low key generation rate, and the lack of a developed on-chip receiver mean more research should be conducted before this technology could be moved towards commercial implementation. At the same time, Sibson et al. provided a comparative study between a silicon-based polarization QKD encoder and a time-bin QKD encoder, using the BB84 protocol in both cases [24]. For the polarization-based QKD, the authors report a QBER of 1.1% with an asymptotic secure key rate of 329 kbps over a 20 km fiber link. For the time-bin encoded states, the authors demonstrate a QBER of ~2.1%. Like the other works discussed, this system is implemented in a laboratory setting and does not operate as an autonomous QKD system.

In 2018, Bunandar et al. demonstrated a proof-of-concept for polarization-based QKD in a field test while using the BB84 protocol [25]. The authors report a QBER of 2% when testing between two neighboring buildings connected by a fiber, with a secret key rate of 1.039 Mbps. When testing

between cities (43 km), they describe a QBER of 2.8% and a secret key rate of 157 kbps. While these error rates are higher than observed in a laboratory setting, this paper represents an important step in the practical implementation of silicon-based QKD. In all of the previously discussed papers, the authors have relied on additional hardware (typically an SLM, q-plate system, or mode sorter) to decode the generated QKD states providing a significant hurdle to commercial implementation. In 2023, Wei et al. described a case study of polarization-based QKD that uses a silicon-based encoder and decoder [26]. The authors use the BB84 protocol, and report a low QBER of 0.50% with a secret key rate of 866 bps over a 150 km fiber link. The authors successfully demonstrate a system that uses no additional hardware to perform the polarization-based QKD, but are limited in the rate at which they can generate and distribute secure keys.

Though this research is useful as a basis and proof-of-concept, these approaches lack the ability to generate the spatial modes required to perform HD QKD. While there has been significant research into the generation or detection of OAM modes through integrated photonics [27-29], these designs have not been considered for implementation in the context of HD QKD as the MUB states cannot be prepared/measured in the required manner. To address this gap, Otte et al. proposed an inversely designed integrated silicon-based device that can be tuned to decode scalar OAM and vector modes, termed a vector beam decoder (VBD) [30]. Like in [26] the VBD also serves as a Vector Beam Emitter (VBE), meaning a closed communication system can be created without the need for additional hardware. This designed device represents the first instance of practical implementation of polarized MUB states for HD QKD. The remainder of this paper is organized as follows. Sect. 2 will describe the process for implementing HD QKD with spatial modes, and discuss the simulated results of the VBD presented in [30]. Following this, Sect. 3 will discuss the fabrication of the VBD, and our experimental process. Sect. 4 will present the results of the experimental characterization of the VBD and compare to the simulated results of [30]. Conclusions and future work will be presented in Sect. 5.

## 2. Background Information for Quantum Key Distribution Communication System

### A. Performing Polarization-Based Quantum Key Distribution

To fully understand HD QKD, it is first important to discuss the implementation of basic polarization-based QKD, which operates on the BB84 protocol [8]. For this, we start with communication between two parties, Alice and Bob, with a potential for an eavesdropper Eve. The bits of information to be transmitted are encoded in the polarization state of the transmitted photons. This can be denoted as the orthonormal basis  $\psi$ , which is comprised of a horizontal and vertical polarization state. Bob can decode Alice's message by measuring in the same basis  $\psi$ . However, in the case of only one basis, this is also true for Eve, and she can avoid detection by intercepting the message sent, measuring it, and cloning it to send to Bob. To avoid this, Alice uses a second basis  $\phi$  which uses the diagonal and anti-diagonal polarization states of the sent photon. It is important that the two bases are MUB states. Alice encodes bit values randomly in one of the two bases, and Bob measures the received photon randomly in one of the two bases. Alice and Bob then exchange via a classical communication channel the encoding and measurement bases used, and discard the data in the cases where they did not match. With no interference from Eve, this leaves them with  $N/2$  bits on average. If Eve interferes, her

measurement will induce errors in their measurements, as she would guess the incorrect basis half of the time, leaving them with an additional  $N/4$  incorrect bits. Alice and Bob then compare their transmitted and received data for a subset of transmission events where they used the same bases. If these differ more than what is expected from noise rates in the communication channel, this indicates the presence of the eavesdropper. Otherwise, the data used in this comparison is discarded, and the rest of transmission is used as a secure key. This process is illustrated below in Fig. 2.1.

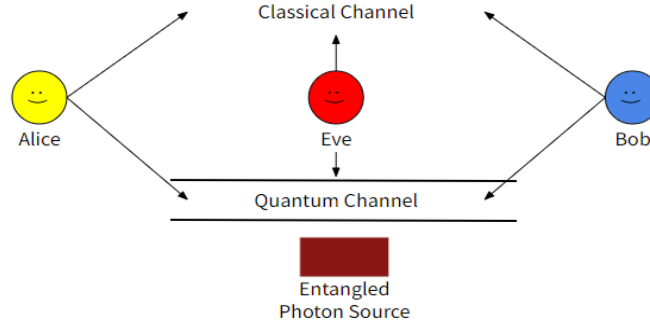


Fig. 2.1. Illustration of QKD communication system.

## B. High-dimensional Quantum Key Distribution with Spatial Modes of Light

To improve the transmission capacity of the system and enhance security, one can increase the dimension by using the spatial degree of freedom (DoF) of the entangled photons. This is done by implementing spatial modes of light in the MUB states. In addition to the polarization DoF described in Sect. 2A, the OAM DoF of the entangled photon is used to create a 4D Hilbert space [31]. The OAM of light is the component of the angular momentum that is dependent on the field spatial distribution and carries a phase vortex structure of the form  $e^{il\theta}$  where  $l$  is the topological charge (number of  $2\pi$  rotations made by the light within one wavelength) and  $\theta$  is the phase angle. The polarization DoF can be combined in the form of the spin angular momentum (SAM) with the OAM DoF that is  $l \pm 1$  to create the first vector mode set, provided in greater detailed in [15] and [32]. In this way, the first basis  $\psi$  is the vector modes formed from the right- or left-circular polarization states with a positive or negative topological charge of 1, while the second basis  $\phi$  is the scalar modes created by the homogenous diagonal or antidiagonal linear polarization states and also carries a positive or negative topological charge of 1. This creates scalar modes shown in Fig. 2.2, where (for each basis) each state corresponds to two bits of information (00, 01, 10, or 11).

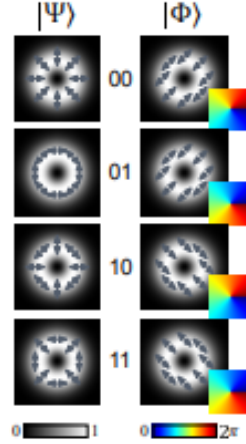


Fig. 2.2. MUB states for 4D QKD represented by spatial modes of light [30].

A transfer matrix can be used to represent the probability of Bob identifying the correct state sent by Alice. As discussed previously, if Alice and Bob randomly select the same basis, Bob will always identify the sent state correctly. If there is a mismatch in the bases, Bob will correctly identify the sent state 25% of the time. This is represented in the top-right and lower-left corners of the transfer matrix. After transmission, Alice and Bob still communicate via a classical communication channel and like previously, they should be left with  $N/2$  information bits after discarding the errors. If there is significantly more error than this, it likely indicates the presence of an eavesdropper.

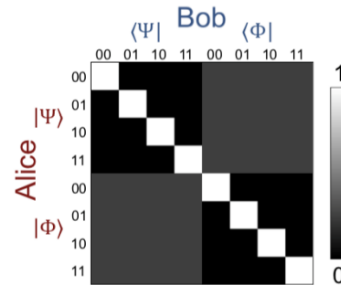


Fig. 2.3. Ideal transfer matrix for communication between Alice and Bob [30].

### C. Design and Implementation of the Tunable Vector Beam Decoder/Encoder

For practical implementation of HD QKD with spatial modes, it was necessary to create a device that was capable of both preparing and measuring all of the desired MUB states with the use of tunable input/output waveguides. Designing a nanophotonic structure to realize this goal is a challenging task, leading the authors to apply inverse design techniques. Nanophotonic inverse design is the computational design of nanophotonic structures using gradient-based optimization. As it would be impossible to sweep the full space of possible designs given the number of controllable variables, a gradient is used to guide the design process towards a desired output [33, 34]. In this case, the authors used adjoint optimized inverse design to create the device, with the goal of forming the MUB states in the transverse electric field components of the VBE

emission. They optimized the structure to take a waveguide mode as an input and then generate a beam through the emitter [30].

An illustration of the VBE/VBD is provided below in Fig. 2.4. The structure is designed to be comprised of air-clad 220 nm thick silicon on an insulator. The authors designed the VBE/VBD in a way so that each of the input wave guides (A-D) generates one of the four scalar MUB states  $|\phi\rangle$ , shown below in simulation in Fig. 2.5. In the case of the vector mode MUB states  $|\psi\rangle$ , these can be generated in a combination of the different input waveguides (A-D) in conjunction with phase modulation of each waveguide [30]. These states are shown below in Fig. 2.6.

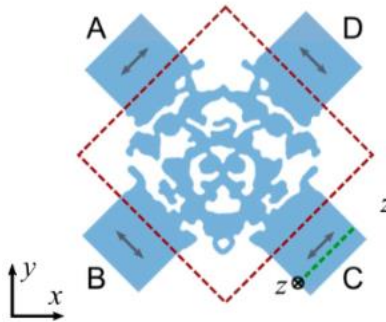


Fig. 2.4. Illustration of inversely designed VBE/VBD structure [30].

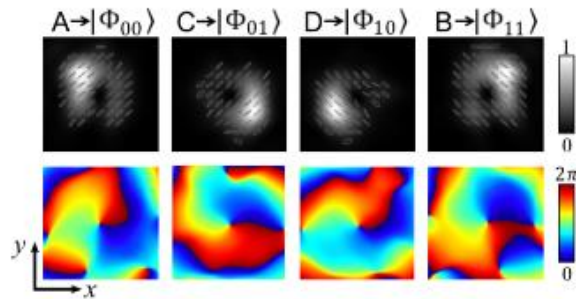


Fig. 2.5. Simulated scalar MUB states generated by input A, C, D, and B, respectively [30].

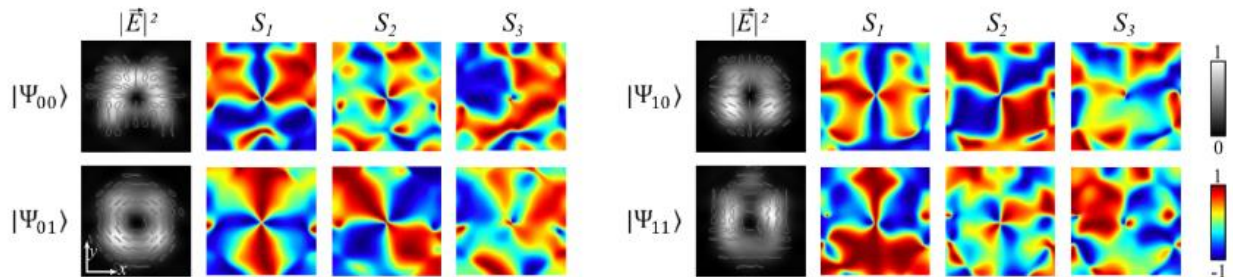


Fig. 2.6. Simulated vector MUB states generated by combining inputs A-D and shifting the phase of the input light [30].

#### D. Simulated Results of Tunable Vector Beam Emitter / Vector Beam Decoder

Following the design and simulation of the tunable VBE/VBD device, the authors investigated the simulated performance and security of the system. In the first case, the authors use a simulated 2D MUB state system where Alice sends her information using the VBE, and Bob decodes using a basis that is 2D polarized, representing a more traditional QKD scheme for easier comparison. The authors report a quantum error rating of 0.057 and an information capacity per photon of 1.189. The resulting transfer matrix is provided below in Fig. 2.7a and demonstrates good alignment with the theoretical values discussed in Sect. 2C. In the second case, the authors look at the simulated 3D MUB states case, where Alice is represented by the VBE and Bob is represented by the VBD. In this case, the authors demonstrate significant improvements in the security of the system and report a quantum error rating of only 0.004 and an information capacity per photon of 1.914. The transfer matrix for this case is presented in Fig. 2.7b, which demonstrates less perturbations than in the first case and better alignment with the theoretically predicted values due to the implementation of the 3D MUB states [30].

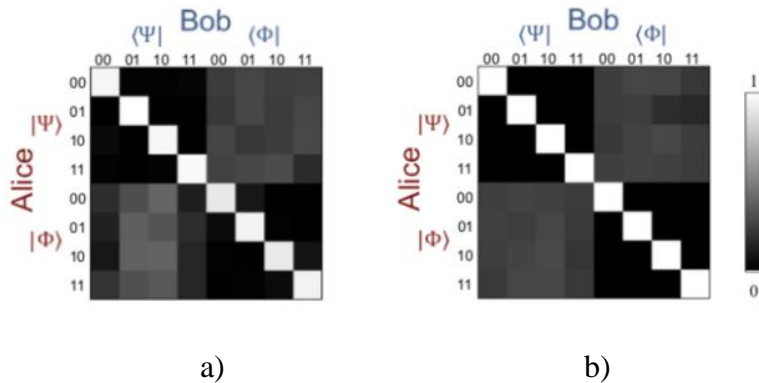


Fig. 2.7. a) Transfer matrix for 2D MUB states and b) transfer matrix for 3D MUB states [30].

### 3. Experimental Process

#### A. Device Fabrication

Fabrication of the VBE/VBD device was completed by Dr. Giovanni Scuri and Sungjun Eun and Sect. 3A was prepared in consultation with them. The devices were fabricated with a silicon-on-insulator (SOI) wafer with a 220 nm thick silicon layer on a 2 mm buried oxide layer. A 300 nm thick ZEP520A resist was spun on the SOI chip and then it was exposed with electron-beam lithography (Raith EBPG 5200+). The pattern for the VBE/VBD was transferred to the silicon layer using the Oxford Inductively Couple Plasma Etcher (ICP-RIE) with  $\text{HBr}/\text{Cl}_2$  gas. After the etching, the resist was stripped with Microposit Remover 1165 and the chip was cleaned with acetone and isopropyl alcohol. The VBE/VBD structure (Fig. 3.1a) is  $3 \times 3 \mu\text{m}$  in size, and has  $1.5 \mu\text{m}$  input waveguides (Fig. 3.1b). The inverse-design process of the structure is given in greater detail in [30] and follows the steps outlined in [34]. The device also uses inversely designed input/output gratings to maximize coupling efficiency, shown in Fig. 3.1c. The gratings were designed following the steps outlined in [35]. Fig. 3.1d provides an image of the entire structure.

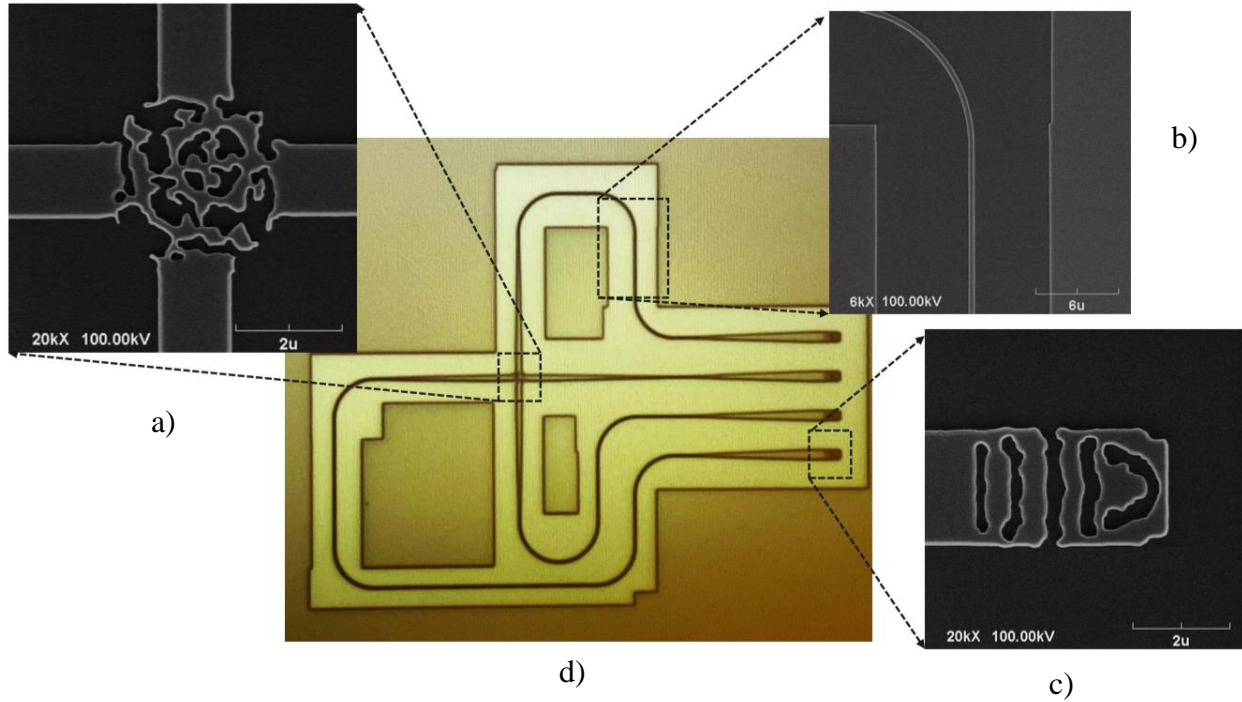


Fig. 3.1. SEM images of a) inversely designed VBE/VBD grating, b) a waveguide, c) inversely input/output grating with approximate location on the chip, and d) the entire structure.

### B. Measurement of Vector Beam Decoder Device

As discussed in Sect. 2C, it was possible to use our fabricated device as either a VBE or a VBD. In the case of the VBE, we could send a signal to the device inputs (A-D) generating all of the MUB states as previously discussed. In this configuration, the emitter structure would emit the generated beam, which could be decoded in this proof-of-concept using a combination of half or quarter waveplates and a q-plate. However, as the chip would perform equally well as a VBD, we determined it was easier to measure and generate the experimental transfer matrix in this configuration. Therefore, we used an encoder system, the combination of either half or quarter wave plates and a q-plate, to generate the desired MUB state, which was focused onto the decoder structure of the VBD. It is important to note that these focused scalar and vector modes generated by the encoder system are only approximations of the MUB states of the VBD. Due to the inverse design of the VBD, the transverse components of the fields match the transverse components of VBD modes. However, the longitudinal components of the VBD and the focused encoder fields differ from one another. Focusing the encoded beams on the decoder structure of the VBD produced an output signal at the device outputs (A-D). We were also able to use a reference beam to calculate the phase of the output light of the VBD couplers, allowing us to measure all of the MUB states discussed. The methods for generating all of the desired modes from waveplates and the q-plate is given below in Table 3.1 [15]. For the vector modes, two half waveplates (HWP) are used and for the scalar modes, two quarter waveplates (QWP) are used. The encoder system used is illustrated below in Fig. 3.2.

Table 3.1. Generation of desired spatial modes from horizontally polarized light. Angles  $\alpha$  and  $\beta$  are defined from the horizontal [15].

Vector Modes $ \psi\rangle$			Scalar Modes $ \phi\rangle$		
Bits	$\hat{J}_\lambda(\alpha_1)$	$\hat{J}_\lambda(\alpha_2)$	Bits	$\hat{J}_\lambda(\beta_1)$	$\hat{J}_\lambda(\beta_2)$
00	0	-	00	$-\pi/4$	0
01	$\pi/4$	-	01	$\pi/4$	$\pi/2$
10	0	0	10	$-\pi/4$	$\pi/2$
11	$\pi/4$	0	11	$\pi/4$	0

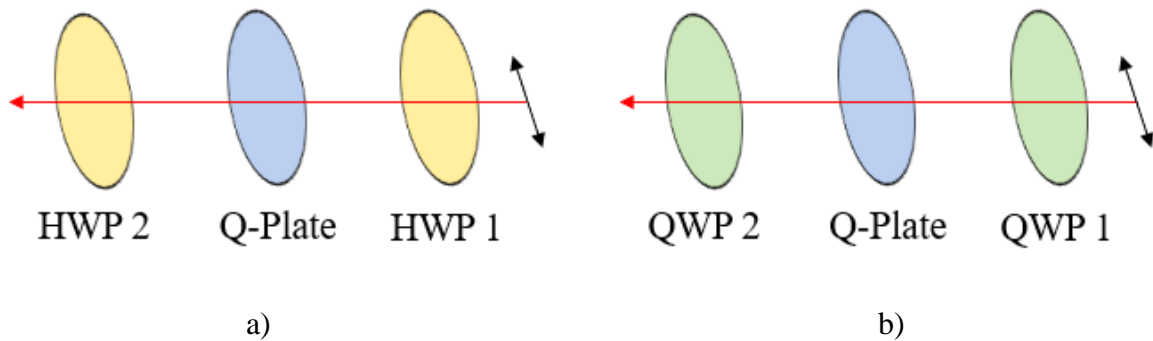


Fig. 3.2. Illustration of encoder system for a) vector modes and b) scalar modes

### C. Experimental Set-up

Our experimental set-up, with a top-down view provided below in Fig. 3.3 and an image shown in Fig. 3.4, uses a 300mW laser at 1550nm as the signal source. This wavelength was selected as it is one of the principal wavelengths widely used in IR communication systems. The laser light is propagated through a 4F lens system comprised of one lens with a 200mm focal length and another with a 150mm focal length in order to magnify the collimated beam, generating a smaller beam at the plane of the VBD. A 512 x 512-pixel SLM is used as a diffraction grating to isolate a Gaussian mode to use as the signal to be encoded. The desired scalar OAM or vector beam is generated using an encoding system comprised of either two QWPs (in the case of the scalar OAM beams) or two HWPs (in the case of the vector beams) with a q-plate in the middle. This allows us to test the proof-of-concept of the VBE/VBD system without needing to use more than one fabricated chip. In practical implementation, the encoding system would be replaced by a VBE where the input modes could be referenced to generate the desired spatial modes. Additionally, in the case of the OAM modes, a polarizer is placed after the encoder system to generate the desired modes. The encoded beam is then propagated into the microscope objective, where it is directed towards the center of the VBD, causing the output gratings to light up depending on the encoded input. In the case of the phase modulated cases, a reference beam is included in order to calculate the phase shift. This image is propagated through a polarizer to reduce scattering and improve the signal to noise ratio (SNR) of the image. Finally, this is collected by a lens system comprised first of a lens with a focal length of 60 mm and second with a lens with a focal length of 200 mm to magnify the

image of the coupler output. This is visualized using an IR camera with a resolution of 320 x 256-pixels. Additionally, our set-up includes a white light source that was sent through the microscope objective to allow us to see and adjust the laser light placement at the plane of the VBD. The image of the VBD chip without the laser is provided in Fig. 3.5.

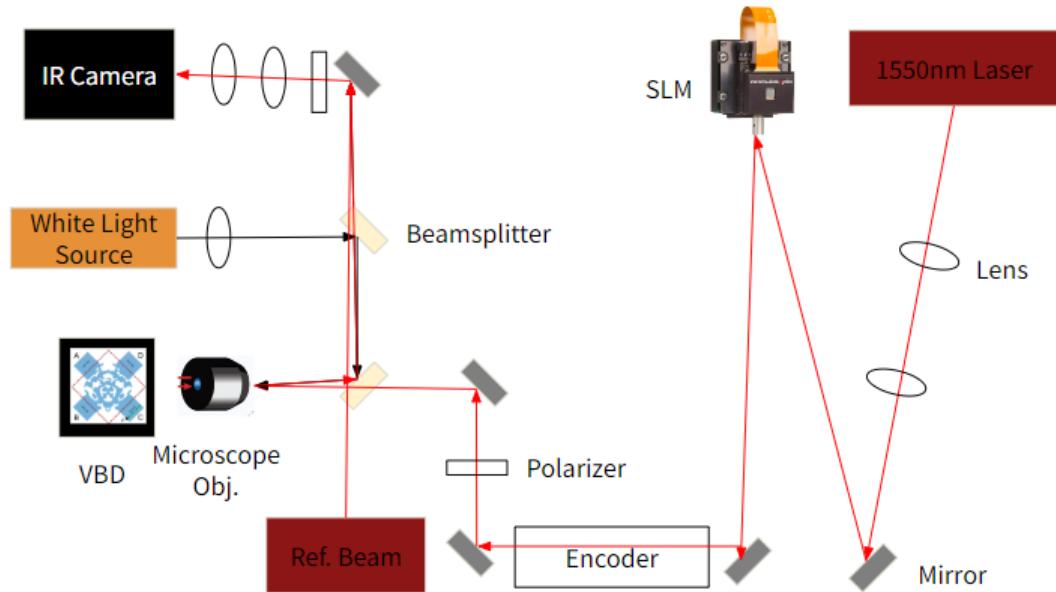


Fig. 3.3. Top-down view of experimental set-up for the characterization of the VBD featuring a 1550 nm laser, 4F lens system for magnification, 512 x 512-pixel SLM, encoder system, microscope, VBD chip, polarizer, 200mm lens, and an IR camera.

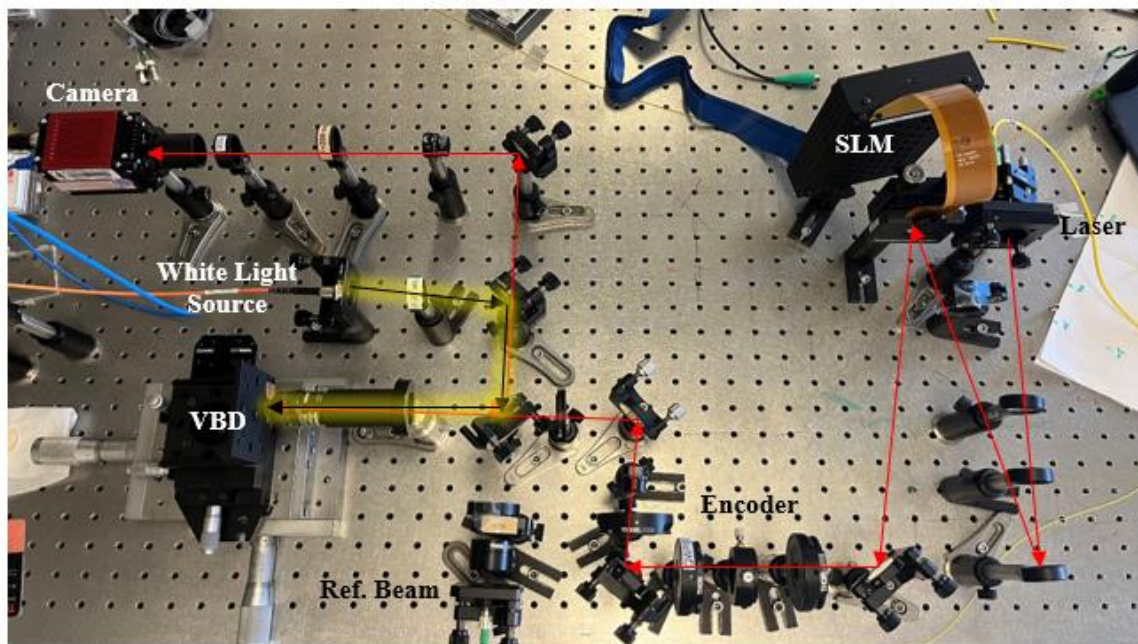


Fig. 3.4. Image of experimental set-up.

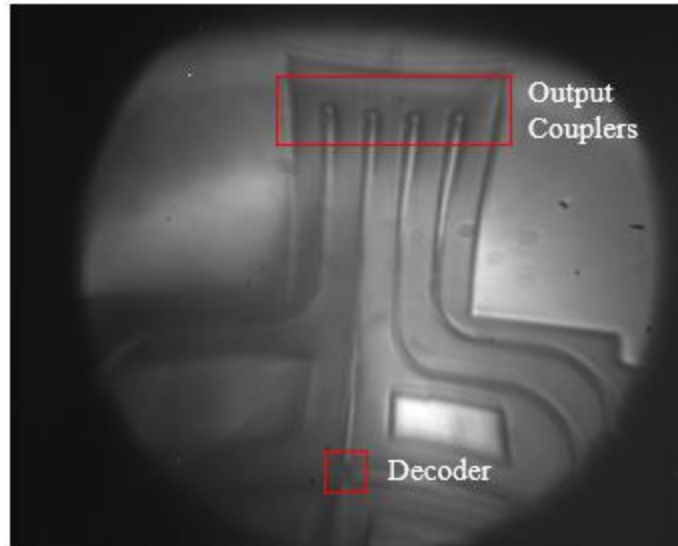


Fig. 3.5. Static image of VBD in the IR camera without the laser turned on.

#### 4. Analysis and Results

To fully characterize the experimental VBD, it was necessary to investigate all possible combinations of what Alice and Bob measure. This is generally recorded in a transfer matrix, which was discussed for the simulated results in Sect. 2D. The transfer matrix provides output values for the cases where Alice and Bob select either the same basis (top-left, bottom-right) or different bases (top-right, bottom-left). To generate an experimental transfer matrix, we used the encoder system outlined in Sect. 3B to generate all eight input MUB states. This arises from creating the four scalar OAM modes ( $|\phi\rangle$ ) and the four vector modes ( $|\psi\rangle$ ) according to Table 3.1, which are then tightly focused onto the VBD. Fig. 4.1 provides images of the intensity of each input beam alongside the bits they correlate to.

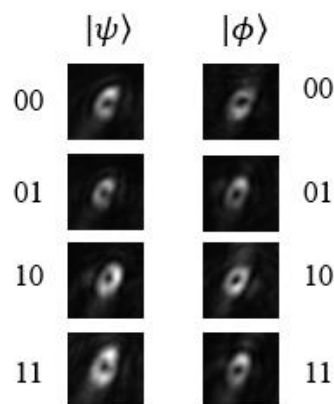


Fig. 4.1. Intensity of all input MUB states prepared using the encoder system.

To verify the intended transverse polarization structure per input beam, a polarizer was placed after the encoder system and rotated. This approach allowed us to qualitatively evaluate the beam's characteristics. This is of particular importance for the vector modes, which show a transverse

variation in polarization. We show example images of this evaluation for  $|\psi\rangle_{00}$  in Fig. 4.2, but all of the input beams were verified in this manner. In Fig. 4.2a, we look at the beam with the polarizer set to a horizontal polarization setting ( $0^\circ$  transmission), which ideally creates two lobes with a vertical separating them through the middle. In Fig. 4.2b, we look at the beam with a vertical polarization setting ( $90^\circ$ ), which ideally creates two lobes with horizontal separation. In Fig. 4.2c and Fig. 4.2d, the polarizer is set to  $45^\circ$  and  $-45^\circ$  respectively, which should create diagonally separated lobes. In the case of Fig. 4.2c, the lobes should be diagonal, and in the case of Fig. 4.2d, they should be antidiagonal. In all cases, we saw what we were expecting to see, validating our encoder set-up and the following results. However, it is important to note that as we focus our encoded beams through the microscope objective, any radial components create extra electromagnetic wave components in the  $z$ -direction. These components were not present in the simulated results shown in Fig. 2.7a and deviate from the  $z$ -components which are considered in Fig. 2.7b. From this expect deviations between these matrices and our final transfer matrix. To more accurately compare our experimentally-generated transfer matrix, we create a simulated transfer matrix assuming the decoding of ideal focused scalar and vector beams ( $NA = 0.9$ ) by the VBD. This matrix is provided in Fig. 4.7a.

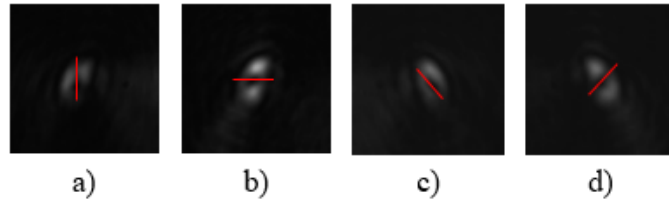


Fig. 4.2. Verification of input vector beam  $|\psi\rangle_{00}$  where each image corresponds to a different angle on the polarizer placed after the encoder system: a)  $0^\circ$ , b)  $90^\circ$ , c)  $45^\circ$ , and d)  $-45^\circ$ .

Having verified our input beams, we then collected images of two cases for each of them following careful adjustment of the focused input beam onto the decoder structure. The first case was the output intensity of the four couplers (outlined in red), and we present the recorded images in Fig. 4.3, for the case of the  $|\phi\rangle$  basis and in Fig. 4.4 for the case of the  $|\psi\rangle$  basis. The output intensity of couplers allows us to extract the right-hand side of the transfer matrix (bottom-right quadrant  $\langle\phi|\phi\rangle$  and top-right quadrant  $\langle\psi|\phi\rangle$ ). Each of the output couplers correspond to the measurement of one of the scalar MUB state. Hence, we isolate the coupler locations in the images and calculated the mean intensity over an area of  $5 \times 5 \text{ px}^2$ , which is then provided in the components of the transfer matrix. From the simulated ideal transfer matrix (Fig. 4.7a) we see that we expect to see maximal intensities in one coupler for the scalar modes, and similar intensities across all four couplers in the vector modes. This is because the VBE/VBD device structure is designed such that each coupler corresponds to one the scalar OAM modes and equal combinations of all couplers with extra phase shifts correspond to vector modes. Qualitatively, we see this behavior in Fig. 4.3 and Fig. 4.4. However, it is worth noting there is some cross-talk present in the images shown in Fig. 4.3, which was expected from the simulations performed. Additionally, we can expect some experimental deviations originating from the fabrication of the device as well as the generation of scalar and vector modes by the encoder system as discussed in Sect. 2B.

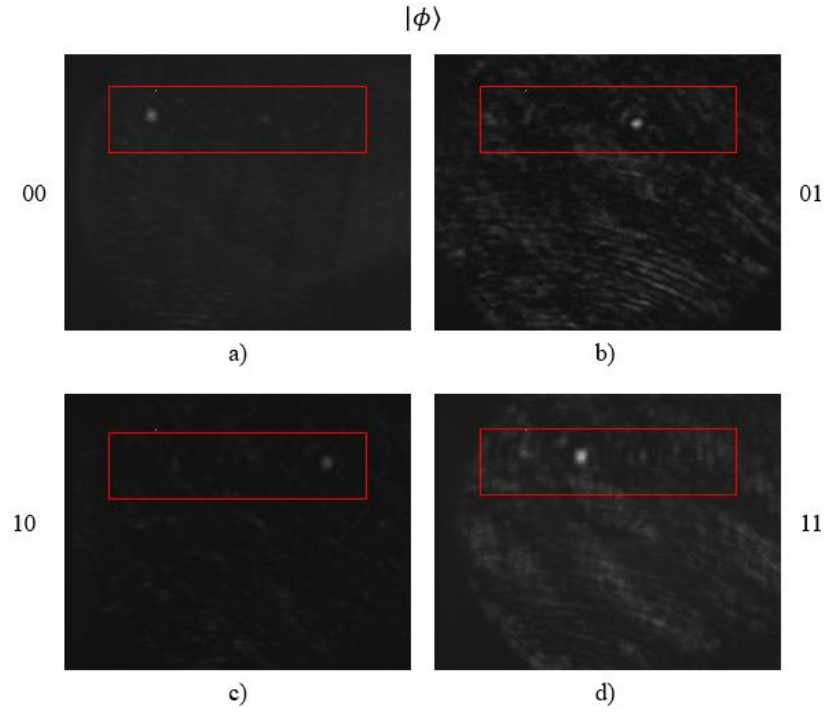


Fig. 4.3. Output images of the intensity at the output couplers with the input of the  $|\phi\rangle$  basis where a) corresponds to 00, b) 01, c) 10, and d) 11.

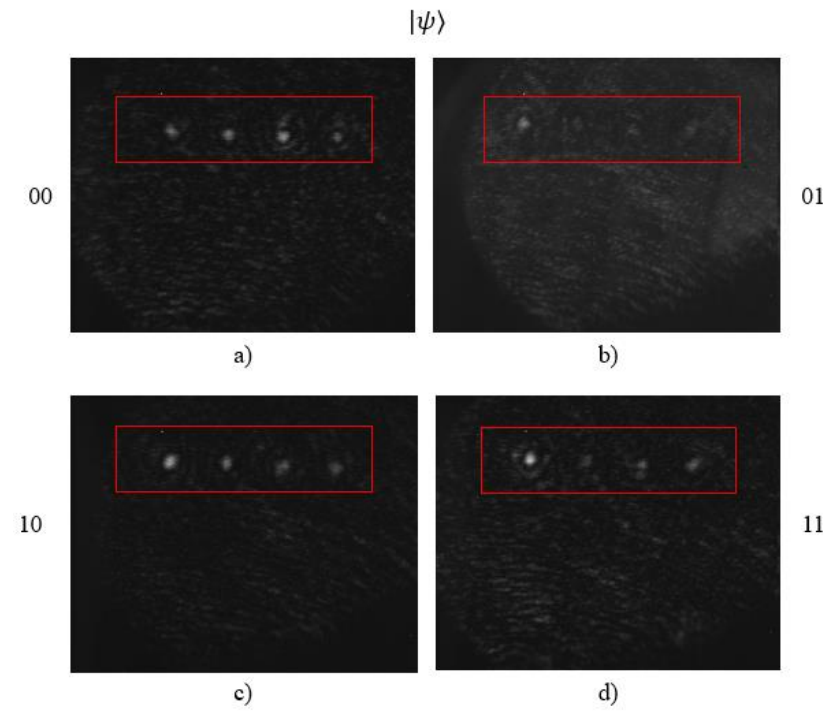


Fig. 4.4. Output images of the intensity at the output couplers with the input of the  $|\psi\rangle$  basis where a) corresponds to 00, b) 01, c) 10, and d) 11.

To generate the left-hand side of the matrix, we collected images of a second case, in which we utilized a reference beam (which was approximately a plane wave) to create interference lines at the coupler output. Similar to above, Fig. 4.5 and Fig. 4.6 provide images for each case of the measurements and the output of the couplers is outlined in red. In all cases, the interference lines at the coupler output can be seen. From the interference patterns, we could calculate the relative phase shift at the output of the couplers [36]. Additionally, we know that for creating/measuring vector beams using the VBE/VBD there is a phase shift to be set for each waveguide. Using the intensity and these two phase values per waveguide allows us to calculate an value for each matrix element on the left-hand side. Each matrix element corresponds to the intensity of the sum of the electric fields per output waveguide after considering the described phase shifts.

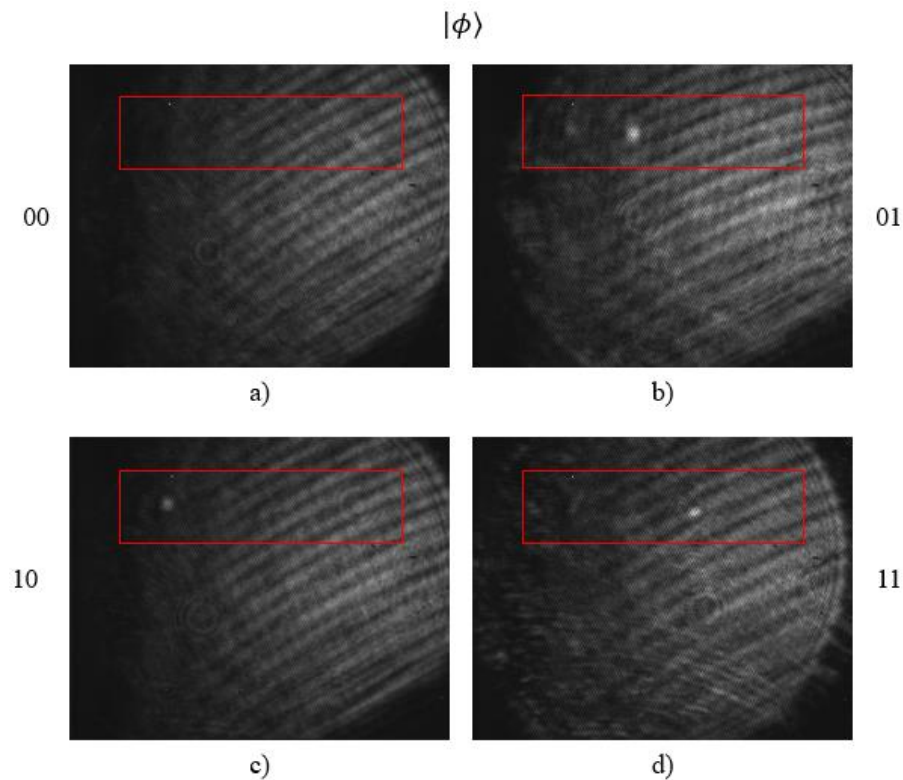


Fig. 4.5. Output images of the intensity at the output couplers with the input of the  $|\phi\rangle$  basis and reference beam where a) corresponds to 00, b) 01, c) 10, and d) 11.

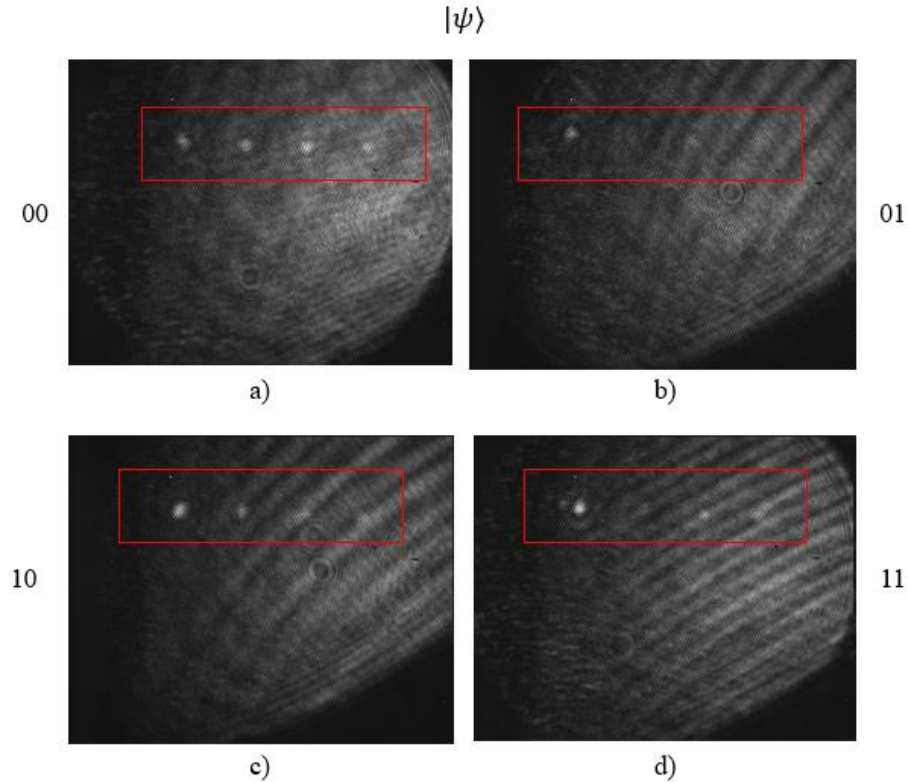


Fig. 4.6. Output images of the intensity at the output couplers with the input of the  $|\psi\rangle$  basis and reference beam where a) corresponds to 00, b) 01, c) 10, and d) 11.

Following this, we generate the experimental transfer matrix. The matrix is then normalized per row by the sum of intensities for equal basis measurements ( $|\langle\psi|\psi\rangle|^2$  or  $|\langle\phi|\phi\rangle|^2$ ); the resulting matrix is shown below in Fig. 4.7b. In comparison to the simulated transfer matrix provided in Fig. 4.7a, we see qualitatively good alignment of the right-hand side with the prediction, just with more (or different) noise. As expected, the intensity values of the top-right quadrant are all around 0.5 when normalized. Additionally, we see the significant contrast between the matched basis and bits in the bottom-right quadrant (near 1 in value) and the matched basis but mismatched bits (near 0). This indicates the device is working as expected, proving the orthogonality of the states in the scalar basis. In the case of the left-hand side, we see more prevalent noise and error present in the transfer matrix when compared to simulation. This is likely due to challenges in precisely calculating the exact phase shifts created by the device – on demand and unintentionally through propagation in the waveguides; additionally, experimental inaccuracies could impact the phase measurements per output coupler, creating errors in the calculation of the matrix elements.

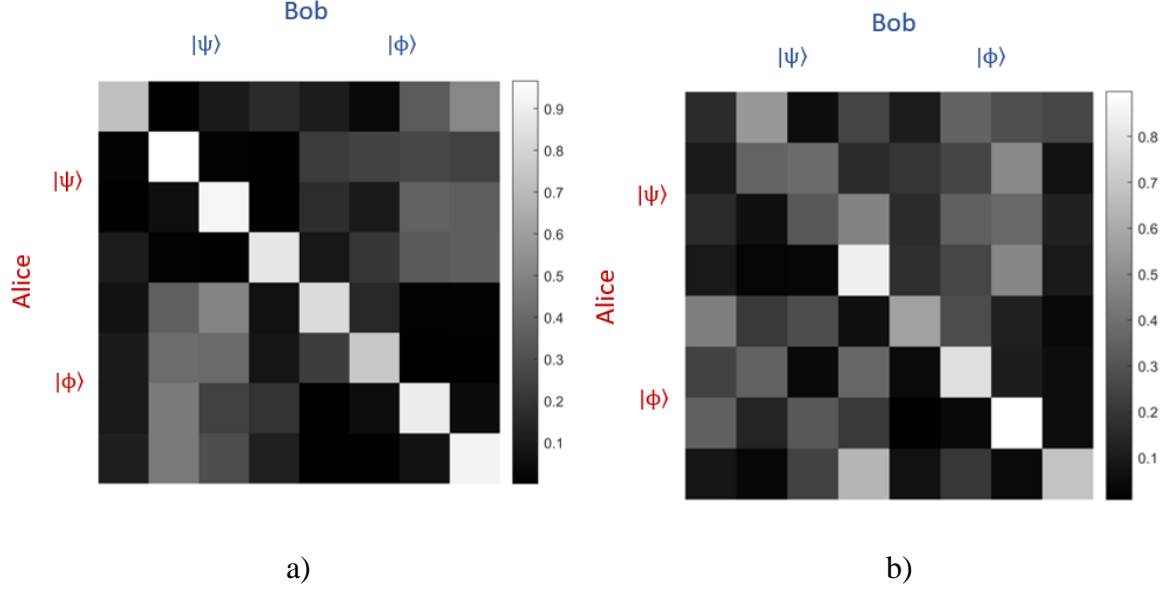


Fig. 4.7. a) Simulated and b) experimental transfer matrix for encoded focused scalar and vector beams (NA = 0.9) measured using the VBD.

Finally, we calculate the performance parameters for both cases and compare to idealized values and the simulated results from [30]. These parameters allow us to perform a security analysis of the QKD scheme. In Table 4.1 we report the quantum error rate  $Q$ , detection fidelity  $F$ , the mutual information  $I_{AB}$  between Alice and Bob, Eve's cloning fidelity  $F_E$ , Eve's mutual information  $I_{AE}$  with Alice, and the information capacity per photon  $R_A$  in bits/photon. We see significant deviation from the simulated results presented in [30] indicating that the mismatch between the focused input beams and the modes of the VBD creates significant error in the results. However, it is important to note that the successfully achieved goal of this work is an experimental proof-of-concept of the VBD, verifying its capability to decode scalar and vector modes in the non-paraxial regime, meaning 3D polarized modes in this case. As shown in simulations of Fig. 2.7b of ref. [30], if Alice and Bob would both implement the VBD for the preparation/ measurement of modes, we observe a significantly optimized transfer matrix; consequently, security values improve with the quantum error rate decreasing and the fidelity increasing close to the ideal values (see Table 4.1).

Table 4.1. Comparison of security values and performance in the ideal case, ideal simulated case, focused-beam simulated case, and experimental case.

	$Q$	$F$	$I_{AB}$	$F_E$	$I_{AE}$	$R_A$
<b>Ideal Values</b>	0	1	2	0.25	0	2
<b>Ideal Simulation [30]</b>	0.004	0.996	1.957	0.306	0.018	1.914
<b>Focused Simulation</b>	0.1393	0.8607	1.1967	0.6195	0.5447	0.3935
<b>Experimental</b>	0.4234	0.5766	0.3459	0.8896	1.4188	-1.3082

## 5. Conclusion and Future Work

This thesis experimentally verifies and evaluates the performance of a tunable VBD for HD QKD utilizing 3D-polarized spatial modes. We verify the capabilities of the VBD by decoding focused scalar OAM and vector modes of light, determining the transfer matrix for the HD QKD scheme. We evaluate the performance on the basis of two transfer matrices, the first in the case of simulating focused ideal scalar and vector modes as input beams and the second by using the experimental results. From these transfer matrices, we calculate the security values and compare to the ideal values and the simulated results presented in [30]. In the case of simulated focused input beams, we report a quantum error rating of 0.1393 and 0.3935 bits/photon. In the experimental case we report a quantum error rating of 0.4234 and -1.3082 bits/photon. The increase in error between our simulated case and experimental case likely results from experimental inaccuracies such as using non-ideal focused input beams or fabrication errors, significantly impacting the output. Additionally, our approach of using a reference beam at the output couplers to calculate the phase shift and generate the left-hand side of the experimental transfer matrix was challenging and measurement errors likely occurred. However, the results presented in this thesis demonstrate a successful proof-of-concept that an HD QKD system utilizing the spatial modes of light could be implemented. Further work should begin by refining the fabrication process for this specific application, and further demonstrate a proof-of-concept by setting up a true key generation scenario. This can be done by fabricating two chips, one to be a VBE and one to be a VBD, representing Alice and Bob, which would also significantly improve security values. An entangled photon could be created using a source like a non-linear crystal, allowing us to demonstrate a working system that uses no additional hardware outside of the VBE/VBD system, entangled photon source, and a classical communication channel. Additionally, the tunable nature of the VBE/VBD device should be experimentally verified, implementing well-established interferometric systems on the chip. As discussed by the authors in [30], the waveguide modes can be phase shifted by small, electrically controlled gold heaters placed alongside the waveguide modes.

## 6. References

- [1] J. L. O'Brien, A. Furusawa and J. Vučković, "Photonic quantum technologies," *Nature Photonics*, vol. 3, no. 687, 2009.
- [2] H.-K. Lo, M. Curty and K. Tamaki, "Secure quantum key distribution," *Nature Photonics*, no. 8, pp. 595-604, 2014.
- [3] H.-K. Lo and H. F. Chau, "Unconditional security of quantum key distribution over arbitrarily long distances," *Science*, no. 283, pp. 2050-2056, 1999.
- [4] V. Scarani, H. Bechmann-Pasquinucci, N. Cerf, M. Dušek, N. Lütkenhaus and M. Peev, "The security of practical quantum key distribution," *Rev. Mod. Phys.*, no. 81, pp. 1301-1350, 2009.
- [5] W. K. Wootters and W. H. Zurek, "A single quantum cannot be cloned," *Nature*, no. 299, pp. 802-803, 1982.

- [6] P. W. Shor and J. Preskill, "Simple proof of security of the BB84 quantum key distribution protocol," *Phys. Rev. Lett.*, no. 85, pp. 441-444, 2000.
- [7] V. Scarani and C. Kurtsiefer, "The black paper of quantum cryptography: Real implementation problems," *Theoretical Computer Science*, no. 560, 2014.
- [8] C. H. Bennett and G. Brassard, "Quantum cryptography: Public Key Distribution and Coin Tossing," in *Proceedings of IEEE International Conference on Computing Systems and Signal Processing*, Bangalore, India, 1984.
- [9] J.-P. Chen et al, "Quantum key distribution over 658 km fiber with distributed vibration sensing," *Phys. Rev. Lett.*, no. 128. 180502, 2022.
- [10] Y. Ding, D. Bacco, K. Dalgaard, X. Cai, X. Zhou, K. Rottwitt and L. K. Oxenlowe, "High-dimensional quantum key distribution based on multicore fiber using silicon photonic integrated circuits," *npj Quantum Information*, no. 3, 25, 2017.
- [11] M. Erhard, M. Krenn and A. Zeilinger, "Advances in high-dimensional quantum entanglement," *Nature Reviews Physics*, no. 2, 365, 2020.
- [12] S. Ecker, F. Bouchard, L. Bulla, F. Brandt, O. Kohout, F. Steinlechner, R. Fickler, M. Malik, Y. Guryanova, R. Ursin and M. Huber, "Overcoming noise in entanglement distribution," *Phys. Riv. X*, no. 9, 041042, 2019.
- [13] F. Hufnagel, A. Sit, F. Bouchard, Y. Zhang, D. England, K. Heshami, B. J. Sussman and E. Karimi, "Underwater quantum communication over a 30-meter flume tank," *arXiv*, no. 2004.04821, 2020.
- [14] M. Mirhosseini, O. S. Magaña-Loaiza, M. N. O'Sullivan, B. Rodenburg, M. Malik, M. P. Lavery, M. J. Padgett, D. J. Gauthier and R. W. Boyd, "High-dimensional quantum cryptography with twisted light," *New Journal of Physics*, no. 17, 2015.
- [15] I. Nape, E. Otte, A. Vallés, C. Rosales-Guzman, F. Cardano, C. Denz and A. Forbes, "Self-healing high-dimensional quantum key distribution using hybrid spin-orbit Bessel states," *Optics Express*, no. 26, 2018.
- [16] G. C. Berkhout, M. P. Lavery, J. Courtial, M. W. Beijersbergen and M. J. Padgett, "Efficient sorting of orbital angular momentum states of light," *Phys. Rev. Lett.*, no. 105, 2010.
- [17] G. Milione et al, "4 x 20 Gbit/s mode division multiplexing over free space using vector modes and a q-plate mode (de) multiplexer," *Optics Letters*, no. 40, 2015.
- [18] A. Forbes, A. Dudley and M. McLaren, "Creation and detection of optical modes with spatial light modulators," *Advances in Optics and Photonics*, no. 8, 2016.
- [19] N. K. Fontain, R. Ryf, H. Chen, D. T. Neilson, K. Kim and J. Carpenter, "Laguerre-Gaussian mode sorter," *Nature Communications*, no. 10, 2019.
- [20] J. Wang, F. Sciarrino and A. Laing, "Integrated photonic quantum technologies," *Nature Photonics*, no. 14, 2020.
- [21] A. E.-J. Lim, J. Song, Q. Fang, C. Li, X. Tu, N. Duan, K. K. Chen, R. P.-C. Tern and a. T.-Y. Liow, "Review of silicon photonics foundry efforts," *IEEE J. Sel. Top. Quantum Electron.*, no. 20, pp. 405-416, 2014.
- [22] P. Sibson et al, "Chip-based quantum key distribution," *Nature communications*, no. 8, 13984, 2017.

- [23] C. Ma, W. D. Sacher, Z. Tang, J. C. Mikkelsen, Y. Yang, F. Xu, T. Thiessen, H.-K. Lo and J. K. Poon, "Silicon photonic transmitter for polarization-encoded quantum key distribution," *Optica*, no. 3, 1274, 2016.
- [24] P. Sibson, J. E. Kennard, S. Stanisic, C. Erven, J. L. O'Brien and M. G. Thompson, "Integrated silicon photonics for high-speed quantum key distribution," *Optica*, no. 4, 172, 2017.
- [25] D. Bunandar et al, "Metropolitan quantum key distribution with silicon photonics," *Physical Review X*, no. 8, 021009, 2018.
- [26] K. Wei, X. Hu, Y. Du, X. Hua, Z. Zhao, Y. Chen, C. Huang and X. Xiao, "Resource-efficient quantum key distribution with integrated silicon photonics," *Photonics Research*, vol. 11, no. 8, pp. 1364-1372, 2023.
- [27] T. Su, R. P. Scott, S. S. Djordjevic, N. K. Fontaine, D. J. Geisler, X. Cai and S. J. B. Yoo, "Demonstration of free space coherent optical communication using integrated photonic orbital angular momentum devices," *Optics Express*, no. 20, 9396, 2012.
- [28] Y. Chen, K.-Y. Xia, W.-G. Shen, J. Gao, Z.-Q. Jiao, J.-P. Dou, H. Tang, Y.-Q. Lu and X.-M. Jin, "Vector vortex beam emitter embedded in a photonic chip," *Physical Review Letters*, no. 124, 153601, 2020.
- [29] A. D. White, L. Su, D. I. Shahr, K. Y. Yang, G. H. Ahn, J. L. Skarda, S. Ramachandran and J. Vučković, "Inverse design of optical vortex beam emitters," *ACS Photonics*, vol. 4, no. 10, pp. 803-807, 2023.
- [30] E. Otte, A. D. White, N. A. Günsken, J. Vučković and M. L. Brongersma, "Tunable vector beam decoder by inverse design for high-dimensional quantum key distribution with 3D polarized spatial modes," *arXiv*, no. 2304.12296, 2023.
- [31] E. Otte, I. Nape, C. Rosales-Guzmán and A. Forbes, "High-dimensional cryptography with spatial modes of light: tutorial," *Journal of the Optical Society of America B*, no. 37, A309, 2020.
- [32] A. Holleczek, A. Aiello, C. Gabriel, C. Marquardt and G. Leuchs, "Classical and quantum properties of cylindrically polarized states of light," *Optics Express*, no. 19, 9714, 2011.
- [33] S. Molesky, Z. Lin, A. Y. Piggott, W. Jin, J. Vučković and A. W. Rodriguez, "Inverse design in nanophotonics," *nature photonics*, vol. 12, pp. 659-670, 2018.
- [34] L. Su, D. Vercruyssen, J. Skarda, N. V. Sapra, J. A. Petykiewicz and J. Vučković, "Nanophotonic inverse design with spins: software architecture and practical considerations," *Applied Physics Reviews*, no. 7, 011407, 2020.
- [35] N. V. Sapra, D. Vercruyssen, L. Su, K. Y. Yang, J. Skarda, A. Y. Piggott and J. Vučković, "Inverse design and demonstration of broadband grating couplers," *IEEE Journal of Selected Topics in Quantum Electronics*, no. 25,1, 2019.
- [36] E. Cuche, F. Bevilacqua and C. Depeursinge, "Digital holography for quantitative phase-contrast imaging," *Optics Letters*, vol. 24, no. 5, pp. 291-293, 1999.